



Article

Cite this article: Hernández-Macià F, Gabarró C, Huntemann M, Naderpour R, Johnson JT, Jezek KC (2024). On sea ice emission modeling for MOSAiC's L-band radiometric measurements. *Annals of Glaciology* **65**, e37, 1–14. <https://doi.org/10.1017/aog.2024.38>

Received: 20 December 2023

Revised: 23 July 2024

Accepted: 5 September 2024


Keywords:

Sea ice; sea-ice model; ice geophysics; remote sensing

Corresponding author:

Ferran Hernández-Macià;
Email: fernandezmacia@icm.csic.es

On sea ice emission modeling for MOSAiC's L-band radiometric measurements

Ferran Hernández-Macià^{1,2} , Carolina Gabarró¹, Marcus Huntemann³,
Reza Naderpour⁴, Joel T. Johnson⁵ and Kenneth C. Jezek⁵

¹Institute of Marine Sciences (ICM-CSIC), Barcelona Expert Center (BEC), Barcelona, Spain; ²isardSAT, S.L., Barcelona, Spain; ³Institute of Environmental Physics, University of Bremen, Bremen, Germany; ⁴Sonova AG, Staefa, Switzerland and ⁵The Ohio State University, Columbus, OH, USA

Abstract

The retrieval of sea ice thickness using L-band passive remote sensing requires robust models for emission from sea ice. In this work, measurements obtained from surface-based radiometers during the MOSAiC expedition are assessed with the Burke, Wilheit and SMRT radiative transfer models. These models encompass distinct methodologies: radiative transfer with/without wave coherence effects, and with/without scattering. Before running these emission models, the sea ice growth is simulated using the Cumulative Freezing Degree Days (CFDD) model to further compute the evolution of the ice structure during each period. Ice coring profiles done near the instruments are used to obtain the initial state of the computation, along with Digital Thermistor Chain (DTC) data to derive the sea ice temperature during the analyzed periods. The results suggest that the coherent approach used in the Wilheit model results in a better agreement with the horizontal polarization of the in situ measured brightness temperature. The Burke and SMRT incoherent models offer a more robust fit for the vertical component. These models are almost equivalent since the scattering considered in SMRT can be safely neglected at this low frequency, but the Burke model misses an important contribution from the snow layer above sea ice. The results also suggest that a more realistic permittivity falls between the spheres and random needles formulations, with potential for refinement, particularly for L-band applications, through future field measurements.

1. Introduction

From September 2019 to October 2020, the Multidisciplinary drifting Observatory for the Study of Arctic Climate (MOSAiC) expedition presented an exceptional chance to gather data on sea ice characteristics over the course of an entire year (Nicolaus and others, 2022). In October 2019, the Polarstern anchored itself to an ice floe spanning approximately 2.8 km × 3.8 km in the northern region of the Laptev Sea. To perform an extensive range of measurements from various research teams, a dedicated science camp was established on the drifting ice floe. This expedition offered a unique opportunity to investigate the variability of the sea ice microwave emissivity signature due to seasonal fluctuations, temperature changes, and the shift from melting to freezing periods. In this work, the ETH L-Band Radiometer (ELBARA, Schwank and others, 2010) and the Ultra Wideband Microwave Radiometer (UWBRAD, Johnson and others, 2016) measurements in autumn and winter are analyzed, both being radiometers designed to measure statically due to their size.

When considering frequencies below 2 GHz, the electromagnetic waves can penetrate the sea ice column to a significant depth (Heygster and others, 2014). This level of penetration permits low-frequency radiometers to capture emissions from deeper layers of the ice, including emission from the ocean, compared to higher frequency radiometers like the Advanced Microwave Scanning Radiometer-2 (AMSR-2). Consequently, lower frequency instruments can be utilized to measure the thickness of thin sea ice. Specifically, at L-band (1.4 GHz), the sensitivity to ice thickness typically is within the range of 50 cm to 1 m, depending on the salinity and temperature of the ice (Kaleschke and others, 2012; Maass and others, 2015; Huntemann and others, 2014; Demir and others, 2022b). The utilization of L-band radiometry proves to be an excellent tool for monitoring the thickness of Arctic sea ice due to a significant proportion of the Arctic ice being seasonal and relatively thin, amounting to approximately 70% covering in January (Kwok, 2018). Several satellites are designed for observing passive microwave emission at L-band, such as the ESA's Soil Moisture and Ocean Salinity (SMOS) satellite (Mecklenburg and others, 2009; Font and others, 2010; Kerr and others, 2010), the NASA's Soil Moisture Active Passive (SMAP) satellite (Entekhabi and others, 2010), or the Aquarius carried on the Satélite de Aplicaciones Científicas—D (SAC-D) satellite.

Many radiative transfer models can be used to compute the brightness temperature (TB) of sea ice, and important differences appear when using one or the other. For instance, for layers of comparable thickness to the wavelength, coherence effects between reflected waves may affect the emitted brightness temperature. Furthermore, electromagnetic waves propagating in natural media, including ice and snow, are affected by scattering and absorption while traveling from where they are emitted to the sensor. In this work three different approaches are



analyzed: the Burke model (Burke and others, 1979), which neglects coherence effects and scattering; the SMRT model (Picard and others, 2018), which neglects coherence but considers scattering; and the Wilheit model (Wilheit, 1978), which uses an coherent approach but neglecting scattering. Another key parameter that determines the brightness temperature is the selection of the sea ice permittivity formulation. The most widely used is the Vant empirical formulation (Vant and others, 1978), but another and more theoretical approach which models the brine inclusions as ellipsoids is described by Shokr (1998). In this paper, the different model predictions are compared to measured data to better understand how improvements to sea ice thickness can be achieved.

2. Data collection and management

ELBARA and UWBRAD data collected during the MOSAiC expedition is analyzed throughout this work. These instruments measured during distinct times and at varying locations, which in turn allows analyzing various situations. For the sea ice growth simulation ancillary in situ measurements required.

2.1 ELBARA

ELBARA is an instrument to measure L-band thermal emission (Schwank and others, 2010). For the MOSAiC expedition, it was mounted on a sledge and equipped with a picket-horn antenna and a manual elevation positioner. This antenna has a Field of View (FoV) of $\pm 23^\circ$ at -3 dB sensitivity relative to the boresite pointing at nadir observation angle θ . Because the antenna temperature $T_B^p(\theta)$ measured at horizontal or vertical polarizations deviates from the brightness temperature of the central facet of the footprint, a conversion is used to obtain a representative brightness temperature of the observed footprint. The methodology to perform this conversion and the calibration procedures is described by Naderpour and Schwank (2021).

During the MOSAiC expedition, a total of 25 904 measurements were collected by ELBARA. They correspond to observations during various periods, with a nominal off-nadir angle of 60° and a temporal resolution of 5 min. Each day's data is averaged in order to obtain a day-by-day evolution comparable to the sea ice growth simulation models.

ELBARA observations occurred in the MOSAiC's Remote Sensing (RS) site over three periods: October 29th through November 20th, December 2nd to the 13th, and December 22nd to 30th.

2.2 UWBRAD

UWBRAD is an instrument that observes sea ice microwave emissions at four different frequencies 540, 900, 1380, and 1740 MHz (Johnson and others, 2016). To ease the analysis, in this work only the 1380 MHz channel data is used. No other frequencies are utilized since the focus is on the emission modeling at L-band. Previous works such as Demir and others (2022a) present a thorough study regarding the other channels. The instrument operates with right-hand, circular polarization. Each frequency has a

bandwidth of 125 MHz and 512 sub-channels, with data samples generated every four seconds for 100 ms antenna observation time. The lowest frequency is more sensitive to deeper ice layers than L-band radiometers, allowing for more accurate thickness estimations (Demir and others, 2022a). Additionally, UWBRAD utilizes a Radio Frequency Interference (RFI) mitigation algorithm to remove unwanted signals, allowing operation in unprotected bands.

The instrument was deployed on the ice at the Remote Sensing (RS) site and performed measurements over two periods, on December 4–13, 2019 (Demir and Johnson, 2021a), and January 17–23, 2020 (Demir and Johnson, 2021b). It monitored the sea ice in configurable oblique angles (35 – 50 off-nadir) to measure thermal emission signatures at the different sensor frequencies. The instrument was positioned on a stationary telescoping mast, offering the flexibility to manually adjust its height as needed. The antenna's orientation was precisely controlled by a programmable rotator unit, enabling the monitoring of sea ice from a specified oblique angle. Additionally, this setup facilitated periodic sky measurements for 5 out of every 15 minutes. After the expedition, algorithms for detecting and mitigating RFI were applied to data to eliminate undesired signals from the data collected. The Level 1 data underwent both internal calibration using a noise diode and external calibration utilizing sky measurements, resulting in the processing of the data to Level 2 and Level 3, respectively. In the last phase of data processing, the Level 3 data underwent a smoothing procedure by applying a 100-sample running average. As for ELBARA, UWBRAD data of each day was averaged in order to obtain the day-by-day evolution in the comparison with the modeled outputs.

Measurements of the sea ice internal temperature and salinity profiles, basal growth rates, and snow layer thickness were made by other members of the MOSAiC expedition. The sea ice for the UWBRAD study was characteristic of undeformed, low salinity, second-year ice that was potentially a refrozen melt pond. The ice was covered by a 5–15 cm thick layer of undisturbed snow.

2.3 Ice coring and DTC profiles

In this work, ice cores taken nearby are used, as only a few ice cores were performed in the RS site where the radiometers were deployed. Specifically, the cores from the BioGeoChemistry-1 (BGC1) site (Angelopoulos and others, 2022) are selected, as they were obtained periodically from a nearby location. An overview of the ice cores used in this work can be found in Table 1.

The BGC1 site corresponds to a first-year ice zone that is suspected to have formed from open seawater around October 2019. This may be distinct in some aspects from the mid December RS site ice as described by Demir and others (2022a). However, where necessary, the potential impact of this distinction is discussed and addressed.

Aside from the ice coring profiles, information from digital thermistor chains (DTC) are used to derive the sea ice temperature evolution, and also as a check for the sea ice thickness simulation from CFDD. Concretely, the DTC12 (Salganik and others, 2023a) is used for the first ELBARA period, and the DTC20 (Salganik and others, 2023b) for the rest of the periods.

Table 1. Overview of the BGC1 ice cores used in the work

MOSAiC's event code	Date	MOSAiC's event code	Date	MOSAiC's event code	Date
PS122/1_4-29	2019-10-24	PS122/1_7-78	2019-11-14	PS122/1_11-11	2019-12-10
PS122/1_5-24	2019-10-30	PS122/1_8-22	2019-11-19	PS122/2_15-12	2019-12-15
PS122/1_6-61	2019-11-07	PS122/1_10-39	2019-12-04	PS122/2_20-92	2020-01-18

3. Modeling

3.1 Sea ice growth evolution: cumulative freezing degree days

The Cumulative Freezing Degree Days (CFDD) model is an empirical formulation (Bilello, 1961; Weeks, 2010) which allows computing sea ice thickness growth, based on the following equation:

$$d_{ice} = 1.33(CFDD)^{0.58}, \quad (1)$$

where the obtained ice thickness is in cm. The CFDD variable corresponds to the daily average 2 m air temperature difference with respect to the seawater freezing point of $T_w = -1.8^\circ\text{C}$.

To simulate the sea ice temperature (T_{ice}) along the time evolution, a linear gradient is assumed as a reasonable approximation following Huntemann (2015). Therefore, using the 2 m air temperature (T_{2m}) obtained from the European Centre for Medium-Range Weather Forecasts (ECMWF) Reanalysis v5 (ERA5, Hersbach and others, 2020) model, the ice bulk temperature can be computed:

$$T_{ice} = \frac{T_{2m} - T_w}{2}. \quad (2)$$

Regarding the sea ice salinity (S_{ice}), an empirical relation from Nakawo and Sinha (1981) is utilized:

$$S_{ice} = \frac{0.12S_w}{0.12 + 0.88e^{-4.2 \times 10^{-4}v}}, \quad (3)$$

where $S_w = 33$ is a typical Arctic seawater salinity, and v is the growth rate computed from the simulation itself.

3.2 Radiative transfer models

In this section, three radiative transfer models to compute the brightness temperature, given the permittivity and the conditions of the ice and snow, are presented. The Burke and SMRT models are based on an incoherent approach, while the Wilheit model accounts for the phase of the electromagnetic waves, i.e. it considers coherence effects. However, while the Burke and Wilheit models neglect scattering, the SMRT model does not.

For all the models only four layers are considered: air - snow—ice—water, with the first and the last considered to be semi-infinite. Various conditions are used as inputs, including sea ice thickness, temperature, and salinity. The sea ice temperature and salinity values determine the permittivity, and are also used as input parameters. The snow layer is assumed to be isothermal with the underlying ice layer, non-saline, and a thickness equivalent to 10% of the ice thickness (Doronin, 1971). Lastly, the seawater is treated as a semi-infinite layer and is assumed to have typical Arctic values, with a temperature of -1.8°C and a salinity of 33.

3.2.1 Burke model

The Burke model is based on a radiative transfer model initially presented by Burke and others (1979) for soil microwave emissivity. This model is based on assumption of incoherent power transfer. Moreover, it neglects attenuation and emission within the atmosphere, since it considers that the sky has an isotropic brightness temperature of 5 K. Furthermore, it assumes homogeneity within the layers, with constant permittivity, temperature, and salinity throughout each layer. It also assumes smooth surface layers. Following the derivation described by Burke and others (1979), the modeled brightness temperature in a given polarization is a combination of the radiation emitted by the layered structure and the radiation reflected by the sky. This approach was already

used with ARIEL data by Gabarró and others (2022), being successful in studying the instrument sensitivity to sea ice emission.

3.2.2 Wilheit model

Another option to model the emission of sea ice at L-band is the one based on Wilheit (1978), also originally designed for soil. The main difference with Burke's is that this model does not neglect coherence effects, and also that it naturally considers an infinite number of reflections within the layers. This behavior can occur at low frequencies if there are two or more interfaces in a plane-parallel media, as an electromagnetic plane wave has the ability to interact with its reflected counterpart interfering between them. As discussed by Huntemann and others (2014), coherence can be particularly significant in the presence of a thin snow layer above ice. However it is noted that roughness on any interface (air-snow, snow-ice, or ice-water) can rapidly reduce coherent interactions, such that many past studies have failed to show evidence of significant coherent interactions (Jezek and others, 2019).

3.2.3 SMRT model

The Snow Microwave Radiative Transfer (SMRT) thermal emission and backscatter model offers a variety of configuration options in computing microwave emission (Picard and others, 2018). This flexibility allows choosing between different electromagnetic theories, snow and sea ice microstructure and other parameters. SMRT is a radiative transfer model that does take into account reflections at layer interfaces, but considers incoherent power transfer. Furthermore, it also considers the layers as plane-parallel, horizontally infinite and homogeneous. In this work, SMRT is run selecting the IBA scattering, along with the Polder-von Santen mixing formula considering two types of inclusions: random needles or spheres inclusion for the sea ice permittivity.

3.3 Permittivity modeling

In Vant and others (1978), a linear relationship between the brine volume fraction and the complex dielectric constant is empirically established, and this relationship holds for both first-year and multi-year sea ice. These empirical coefficients can be interpolated to the desired frequency band, in this case 1.4 GHz.

A more theoretical approach considers sea ice as a combination of two dielectric materials: ice and brine. The configuration and orientation of brine inclusions within the mixture, plays a significant role, as studied by Shokr (1998). Two inclusion shapes are examined in this work: spherical inclusions and randomly oriented needle-like inclusions. Harsh conditions during ice formation may result in randomly oriented needle-like inclusions, while smoother conditions with minimal temperature fluctuations can lead to spherical inclusions or vertically oriented needles or ellipsoids (Vant and others, 1978; Shokr, 1998). As the ice gets colder, the brine's salinity increases. Therefore, in empirical models, the salinity is often represented as a polynomial function of temperature (Assur, 1960). Regarding the dielectric mixing formulas, the complex dielectric constants of pure ice and brine are necessary. The dielectric constant of pure ice is dependent on temperature and frequency and can be modeled using the approach described by Mätzler (2006), even though in the given frequency range of observations, the modeled permittivity does not change noticeably based on frequency. On the other hand, the dielectric constant of brine is obtained from Stogryn and Desargant (1985). When considering pure ice as the host material and the brine as well as the inclusions, the expressions for the two types of sea ice inclusions are derived from Shokr (1998).

Figure 1 shows the 1.4 GHz refractive index, divided into its real and imaginary parts, as a function of the sea ice temperature

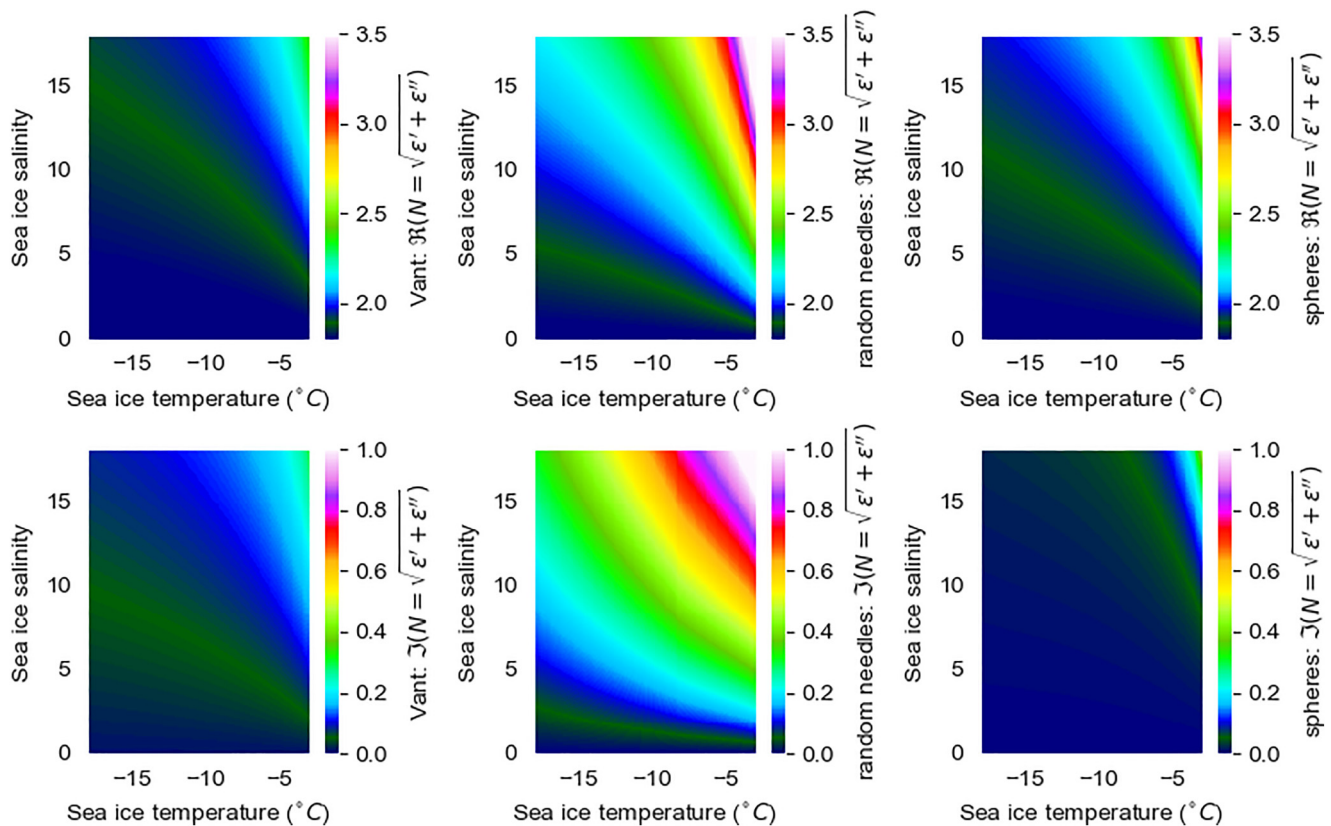


Figure 1. Real (upper) and imaginary (lower) parts of the refractive index at 1.4 GHz for the three described permittivities, Vant, random needles and spheres, as a function of the sea ice temperature and salinity. Reproduction of Figs. 2.1 to 2.3 of Huntemann (2015).

and salinity, for the different permittivity formulations. It should be noted that the refractive index is shown to ease the visualization of the dielectric properties, since it is computed as the square root of the complex permittivity. The reason behind the observed contrast can be understood by examining the analysis provided by Huntemann (2015). These permittivity models can be categorized into three groups based on their levels of absorption: high absorption, moderate absorption, and low absorption. The high absorption category is assigned to the random needles model, which exhibits a high permittivity, that corresponds to an early saturation and emission primarily influenced by surface conditions. The Vant formulation falls under the moderate absorption category due to its lower saturation and intermediate status, depicted by the low permittivity shown in Figure 1 in its both real and imaginary parts. The spheres model presents an intermediate permittivity's real part and an extremely low imaginary part, and it is classified as having low absorption because it does not reach saturation at high thickness levels.

The real part of the complex dielectric constant for the snow layer is obtained from Mätzler (1996), while the imaginary part is derived from Tiuri and others (1984) and Mätzler (2006). The formulation of the complex dielectric constant of the snow is dependent on its density, and a typical value of 0.3 gm^{-3} is commonly used for the Arctic region, as stated by Warren and others (1999). Additionally, the complex permittivity of seawater is acquired from Klein and Swift (1977), assuming a standard salinity value of 33 for the Arctic Ocean.

3.4 Sensitivity analysis

To extend the analysis on the permittivity modeling, the sensitivity study of the brightness temperature as a function of the sea ice thickness for the radiative transfer models combined with the

three presented formulations is shown in Figure 2. An important distinction is evident among the dielectric models regarding the brightness temperature dependence on sea ice thickness, which can reach up to 50 K in some instances. These differences match with the absorption behavior described in Section 3.3. Regarding the radiative transfer models, the two incoherent models, i.e. Burke and SMRT, present a similar behavior, while the Wilheit model enables the possibility of reaching much lower and higher intensities and has the oscillations due to the coherence effects. Furthermore, no differences are observed between the two polarizations of the brightness temperature.

In order to study the intensity dependence on the bulk temperature and salinity of the sea ice layer, Figures 3 and 4 show its dependency for the multiple models. Again there is a clear distinction between the different permittivity formulations, with the Vant and the random needles being more similar while the spheres present much lower intensities for all the simulated sea ice conditions. The radiative transfer models are more similar overall compared to the dependence with the sea ice thickness. However, again higher intensities are reached with the Wilheit model. In this case there is also no differences between the behavior of the two polarizations, except for the fact that the vertical polarization is always higher than the horizontal.

4. Results

ELBARA and UWBRAD data from MOSAiC are analyzed by comparing with model simulations. Prior to computing the microwave emission, the CFDD model is used to simulate the sea ice growth evolution. In many figures, the different models are named with abbreviations. To clarify it, it is noteworthy to mention that the different permittivities, i.e. Vant, random needles and spheres, are depicted by *vant*, *rn* and *sp*, respectively.

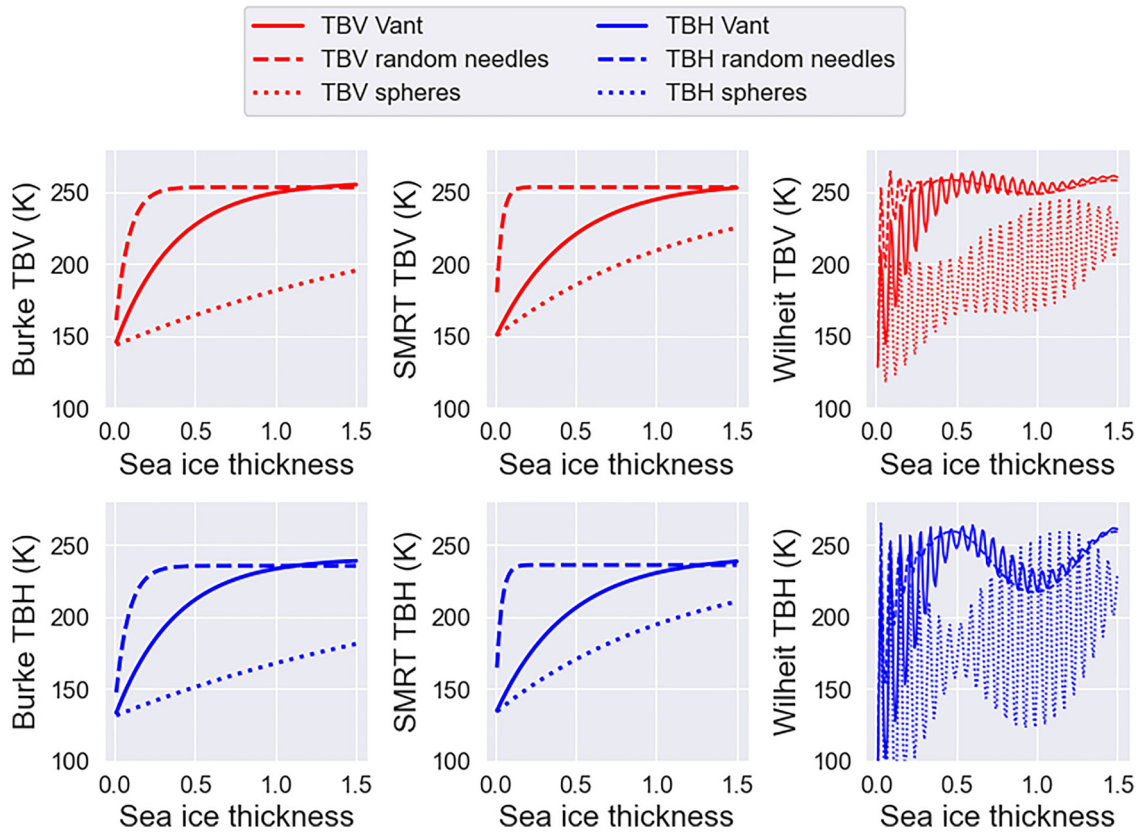


Figure 2. Brightness temperature as a function of the sea ice thickness for the different radiative models, Burke, SMRT and Wilheit, combined with the permittivity formulations, Vant, random needles and spheres. The assumed sea ice temperature and salinity is $T_{ice} = -10^{\circ}\text{C}$, $S_{ice} = 5$, respectively.

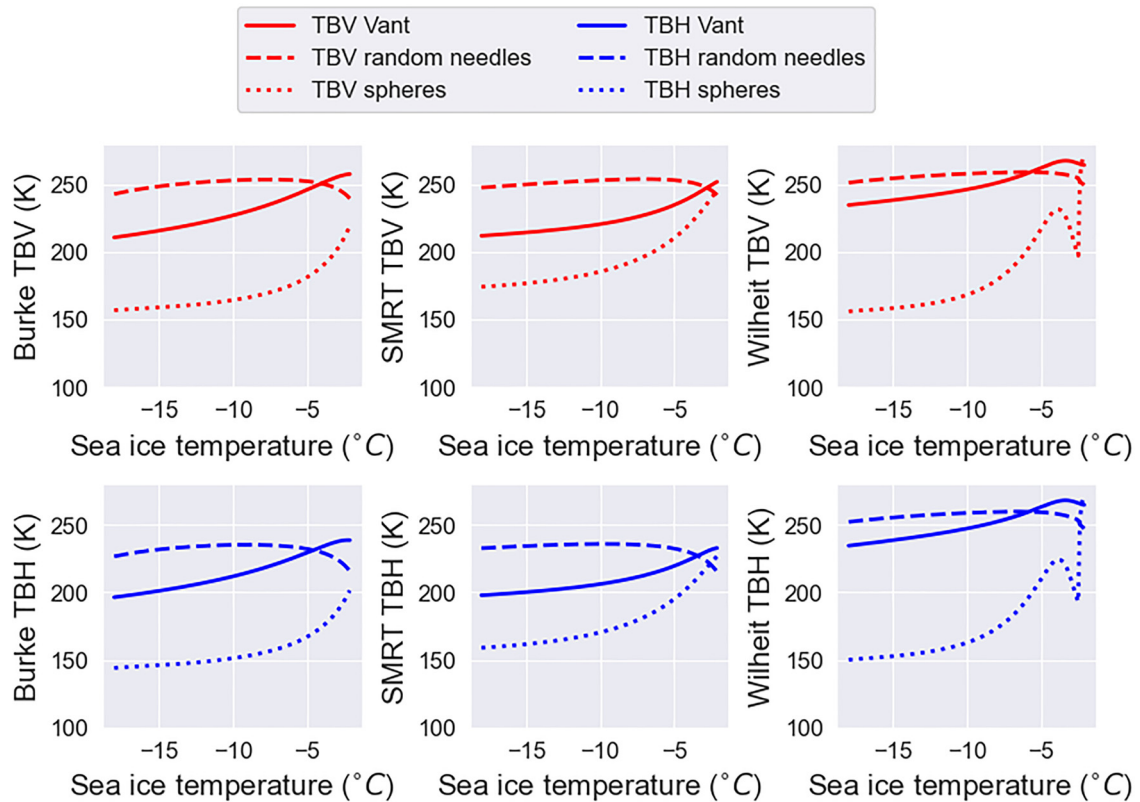


Figure 3. Brightness temperature as a function of the sea ice temperature for the different radiative models, Burke, SMRT and Wilheit, combined with the permittivity formulations, Vant, random needles and spheres. The assumed sea ice thickness and salinity is $d_{ice} = 0.5\text{ m}$, $S_{ice} = 5$, respectively.

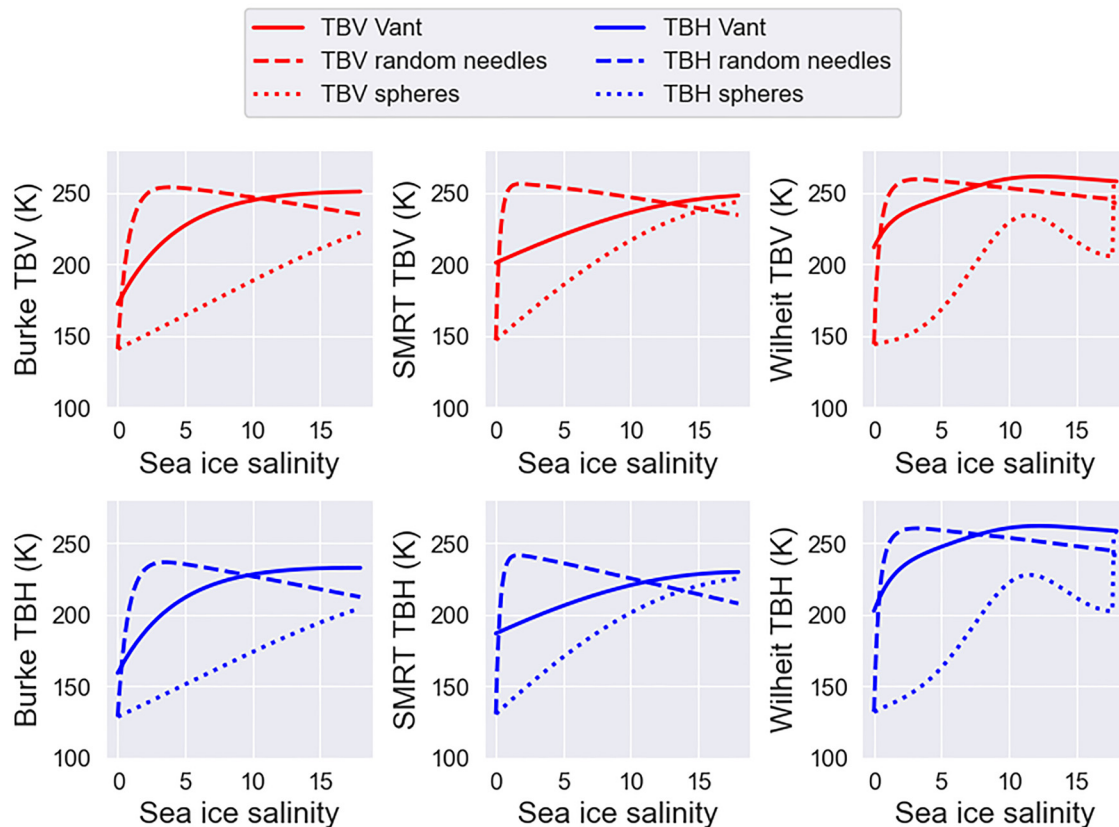


Figure 4. Brightness temperature as a function of the sea ice salinity for the different radiative models, Burke, SMRT and Wilheit, combined with the permittivity formulations, Vant, random needles and spheres. The assumed sea ice temperature and thickness is $T_{ice} = -10^{\circ}\text{C}$, $d_{ice} = 0.5$ m, respectively.

The first two MOSAiC legs took place during autumn of 2019. This period corresponds to sea ice continuously growing. Therefore, static measurements from the L-band radiometers deployed in the ice floe can be compared to the CFDD simulation, which require in situ sea ice conditions derived from ice coring activities, combined with a radiative transfer model to compute the emitted brightness temperature. However, to double-check the conducted simulation, DTC measurements are used to obtain information on the sea ice thickness and temperature evolution during the analyzed periods.

4.1 Sea ice growth simulation: late 2019 and early 2020

Figure 5 shows how the modeled sea ice conditions, thickness, temperature and salinity, evolve during the sea ice growth period until late 2019, along with data from the BGC1 ice coring and DTC profiles. Hereafter, the label CFDD refers to the simulation described in Section 3.1, where the sea ice thickness is computed with the CFDD model itself, the sea ice temperature from the linear gradient assumption using the meteorological data, and the sea ice salinity from the Nakawo and Sinha (1981) formulation. The CFDD simulation is started, for the first period, from the sea ice temperature and salinity conditions extracted from the BGC1 ice core measured on October 24 2019. For the second period, the ice core from December 4 2019 is taken. Finally, for the last period the ice coring performed on December 15 2019 is used. This explains why there is a slight deviation in the sea ice temperature and salinity between the end and the start of the next simulated period.

As expected, the sea ice thickness keeps growing during this time, shown by both the ice coring and the DTC data, also well reproduced by the CFDD model. Regarding the temperature, it reproduces a general decrease in sea ice temperature as freeze-up advances. However, there is a major deviation of the linear

gradient assumption taking the 2 m air temperature data from ERA5. This effect can be produced by the snow layer above (Maass and others, 2015), as it insulates the ice preventing it to reach lower temperatures as those obtained in the CFDD simulation. There is almost no variation through time of the sea ice layer averaged salinity reproduced with the Nakawo and Sinha (1981) formulation, despite a subtle increase observed in early December. This happens because the used formulation determines the salinity of the ice that has grown within a given period, so an stable growth rate such as the observed can produce it.

The sea ice conditions extracted from BGC1 ice cores that were measured throughout these periods, and the DTC installed near the RS site, are also shown in Figure 5. For the latter, the sea ice thickness is derived directly from the difference between the snow-ice and the ice-water interfaces provided by Salganik and others (2023a) and Salganik and others (2023b). Regarding the DTC sea ice temperature, the bulk value is obtained by averaging all the temperatures measured by the thermistor chain sensors within the ice layer.

During November, when sea ice is expected to be growing rapidly, four ice cores and the DTC12 are used as ground truth to study the reliability of the CFDD model. It seems to slightly overestimate the sea ice thickness compared to the ice cores, around 5 cm, but remains near the DTC-derived thickness with a similar general trend. Furthermore, there is a general underestimation compared to the DTC data, compared to both the DTC12 used in the first period and the DTC20 used in the rest, so the simulation lays in an intermediate region between the two in situ sources. Clear conclusions remain difficult because these ground truth data were not measured exactly where the radiometers were measuring, so this variable could be slightly different throughout the ice floe. However, for the sea ice temperature, the major deviation of the CFDD simulation suggests the use of

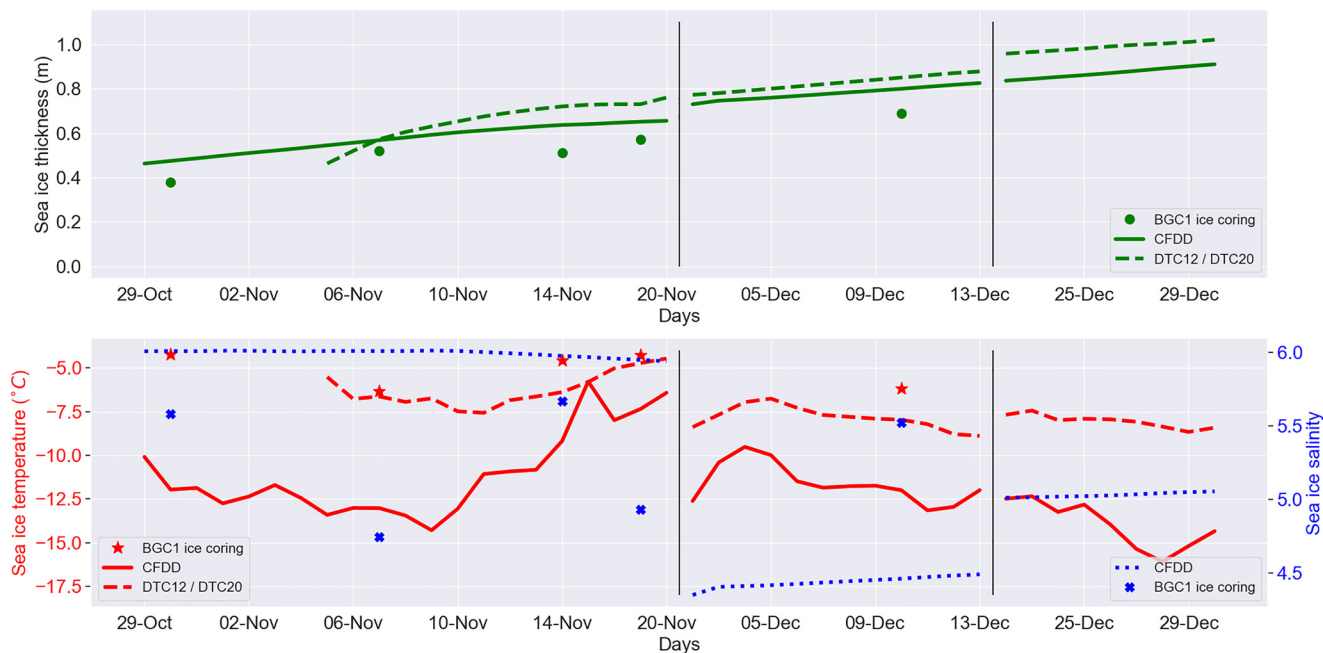


Figure 5. Temporal evolution of the sea ice conditions modeled with the CFDD model during late autumn and early winter 2019/2020 of MOSAiC, along with in situ conditions extracted from BGC1 ice cores and DTC measurements.

the sea ice temperature from the DTC's to compute the modeled brightness temperature, which remain much near the ice coring profiles. Finally, the in situ salinity measurements remain almost constant as also does the model, both around 5. This is further supported by what is shown by Angelopoulos and others (2022), where a complete study of the MOSAiC's BGC ice core data is presented. The sea ice evolution shown there indicates that the salinity had the typical C-shape salinity profile (Cox and Weeks, 1988) in late October, i.e. a higher salinity at the top/bottom and lower in the middle, which slowly changed into a less curved and saline profile. The average ice bulk salinity remain mostly constant near 5, as also shows the Nakawo and Sinha (1981) model and the ice coring profiles.

Therefore, in this work, the sea ice thickness and salinity from the CFDD simulation are combined with the DTC-derived sea ice temperature to compute the modeled brightness temperature. It it should be noted that the gap in the DTC12 data from October 29 to November 5 is filled by subtracting to the CFDD-simulated temperature its mean difference with the DTC12 data, as they are shown to reproduce a similar trend.

Regarding the second period, during which UWBRAD was operational, Figure 6 shows the temporal evolution of the simulated sea ice conditions, using the BGC1 ice core from the January 18 2020 as initial state. Unfortunately, no more ice cores were performed throughout this period, and thus no further insights can be extracted. However, and similarly to the previous periods,

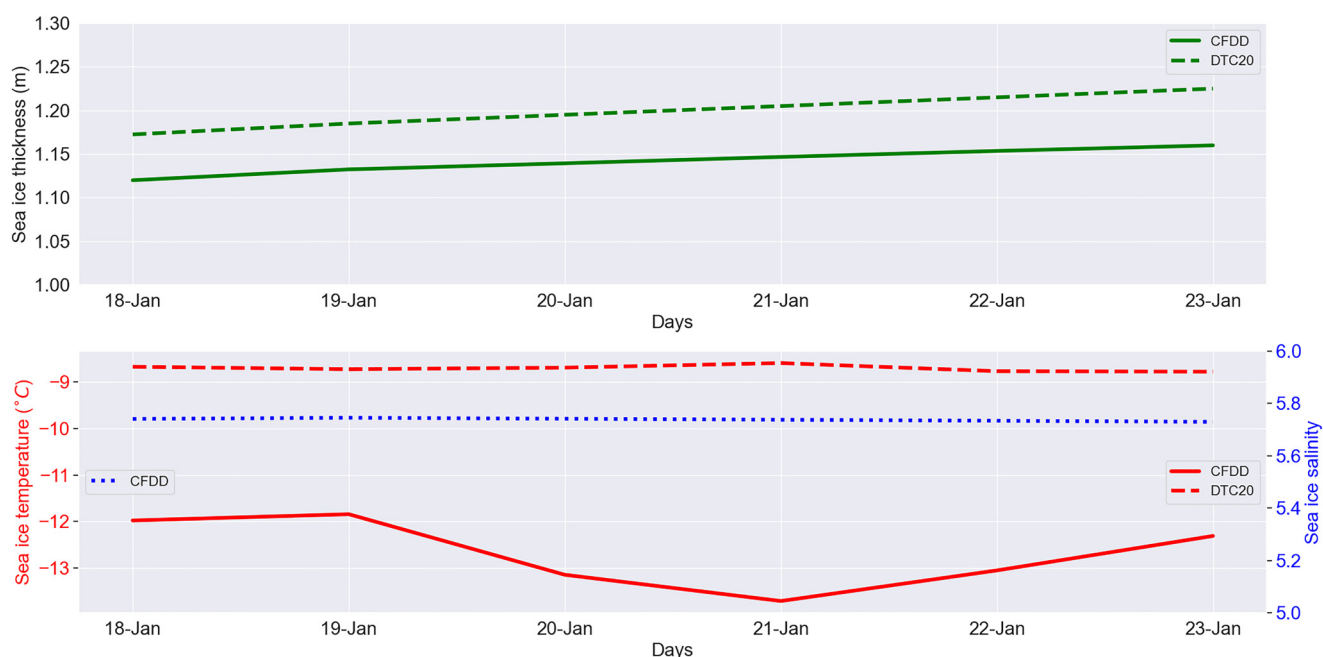


Figure 6. Left: Temporal evolution of the sea ice conditions modeled with the CFDD model during mid January 2020, along with DTC measurements. **Right:** Temporal evolution of the sea ice temperature and salinity modeled with the CFDD model during mid January 2020, along with DTC measurements.

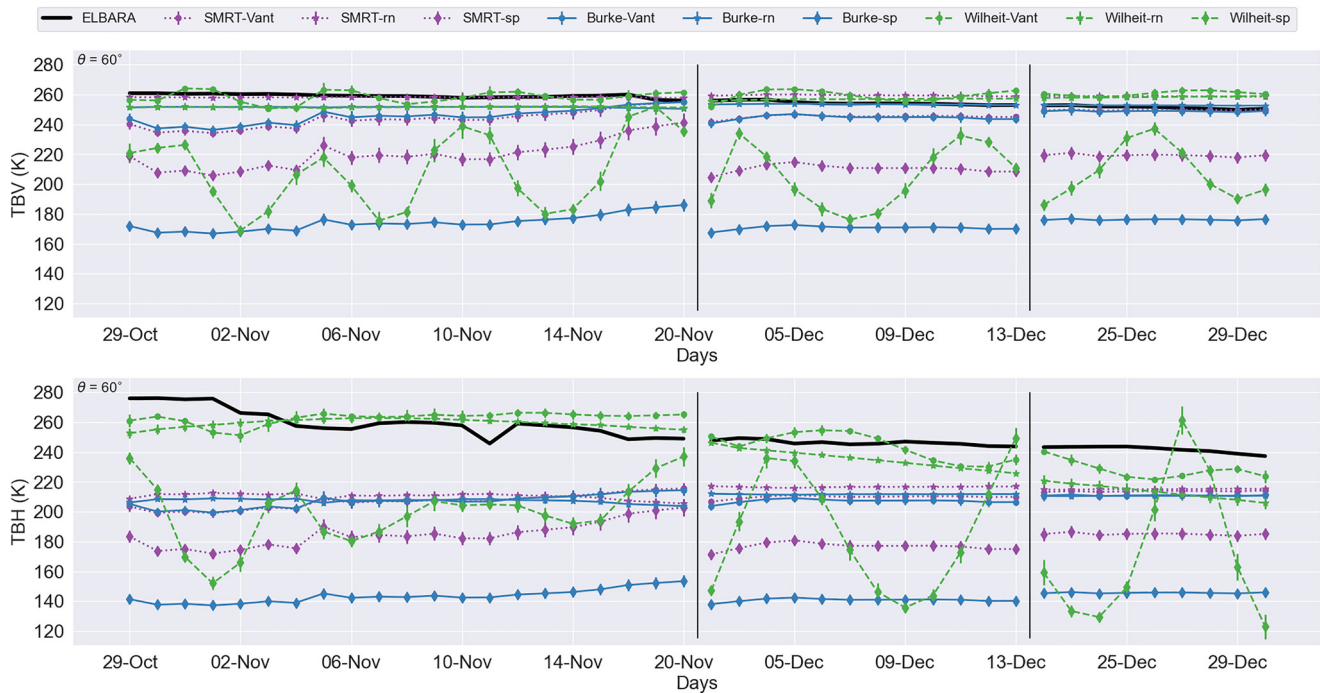


Figure 7. Temporal evolution of brightness temperature, TBV on the upper row and TBH on the lower row, respectively, measured by ELBARA during the sea ice growth period, along with the model simulations.

the CFDD simulation is close to the DTC-derived sea ice thickness, but presents a major deviation for the sea ice temperature, in this case even showing a different trend. The model reproduces the expected trend for ice thicker than 1 m: a much slower growth, less than a centimeter per day. For this period the modeled brightness temperature to be compared with the in situ L-band radiometric data is computed using the same input sources: the sea ice thickness and salinity from the CFDD simulation, along with the DTC-derived sea ice temperature.

4.2 Radiometric data analysis

The three radiative transfer models configured with the different ice permittivities are evaluated for the sea ice growth period measurements of ELBARA and UWBRAD.

The error bars, presented in the subsequent figures, are computed as the root squared difference between the modeled brightness temperature with the DTC-derived sea ice temperature and with the conditions from the CFDD simulation, i.e. from the sea ice temperature derived from the 2 m air temperature by assuming a linear gradient within the ice. The averaged standard deviation of the error bars resulted in around 1.5 K for all the analyzed observations. This low dispersion represents less than 1% of the TB range, showing the stability of the simulations.

4.2.1 ELBARA measurements

The temporal evolution of the sea ice brightness temperature measured by ELBARA during the different periods is shown in Figure 7, along with the models output with the presented permittivities. The results for the vertically-polarized brightness temperature (TBV) are better overall, as all the models considering the Vant and the random needles permittivities have acceptable discrepancies with the observations. The general trend is well reproduced by the models, although for the first days of the simulation there is a deviation: the brightness temperature is slightly reduced while the models show an increase until stabilizing around the measured values. This can arguably be because of

the uncertainty introduced with the ice cores taken as initial state. For the horizontally-polarized brightness temperature (TBH), in early November no model is able to reproduce the large values measured by the sensor, which are not physically realistic for sea ice with water underneath and may indicate a technical issue of the instrument or just RFI-corrupted data. Only the Wilheit model, i.e. the coherent approach, can reach those unusually large measured values, particularly with Vant's permittivity formulation, but not clear evidence of the oscillatory behaviors predicted by the Wilheit model are present in the measured data. For the other periods, all the models present a similar output, considerably lower than the in situ data. However, again the Wilheit model is the closest as it exhibits higher values by including coherence effects.

Figure 8 shows the relative difference computed for each model configuration with respect to the ELBARA measurements during the sea ice growth period, from late October to late December. The Burke and the SMRT models present a similar behavior, as they are both incoherent and the scattering that is considered at SMRT can be neglected at L-band. Nevertheless, the Burke model is generally lower than SMRT, as also shown in Figure 7, particularly when both models consider the Vant or the spheres formulations. Regarding the permittivity, the spherical brine inclusions produce a major difference for both polarizations. However, it is worth mentioning that the combination of the spheres permittivity with the Wilheit and SMRT models result in a better reproduction of the measured data. Focusing on TBV, the three permittivities almost sorted by relative difference with ELBARA are random needles, Vant, and spheres respectively, despite the radiative transfer model used. For TBH specifically, the relative metrics again indicate that the coherent model, combined with the Vant and the random needles models, are the best configurations to reach such large values.

4.2.2 UWBRAD measurements

A similar analysis can be conducted for the 1380 MHz channel measurements of UWBRAD. It should be noted that for every

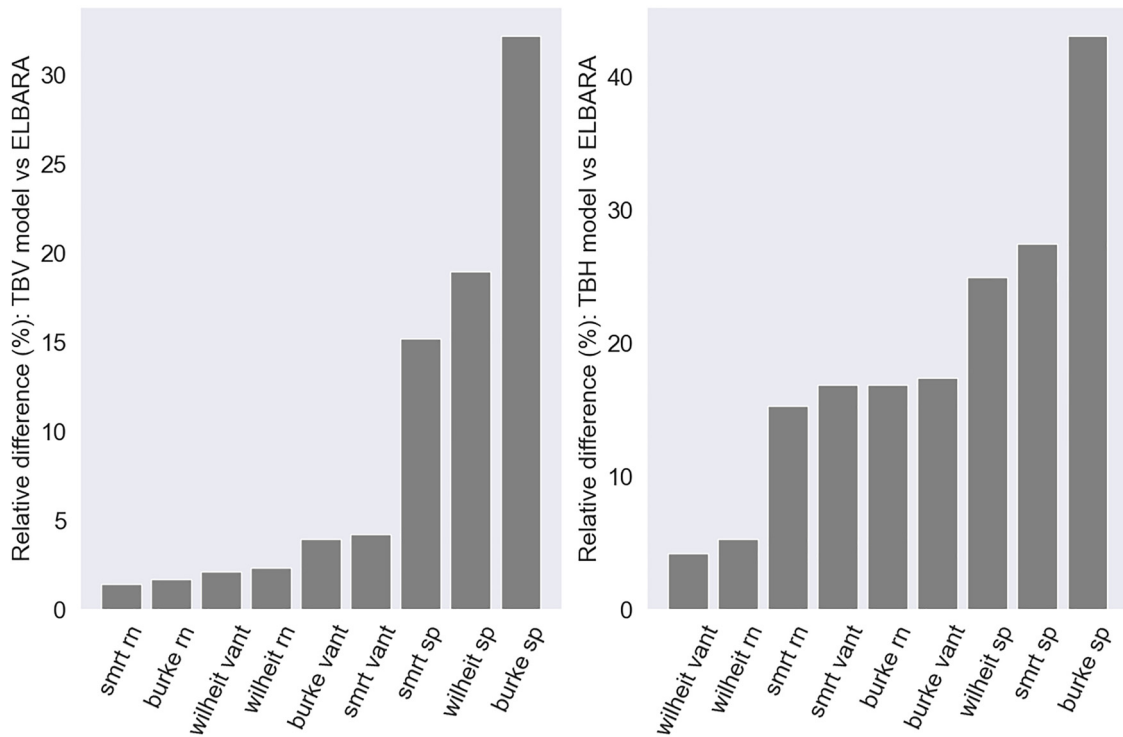


Figure 8. Left: Relative difference of the modeled TBV from different models with respect to the in situ ELBARA measurements during the sea ice growth period. **Right:** Same but for TBH.

incidence angle at which UWBRAD conducted measurements during this period (see Fig. 6 from Demir and others, 2022a), and because of the wideness of the UWBRAD antenna, its antenna pattern is projected onto the surface to get a range of observation angles and then the modeled sea ice brightness temperatures at the resulting varying incidence angles are integrated over the pattern. Figure 9 shows the temporal evolution of the modeled brightness temperature and the in situ measurements from UWBRAD in early December. Every model is able to reproduce the subtle increasing trend on the brightness temperature measured by the instrument, although the Burke and the SMRT models are the best, except when assuming the spheres permittivity. Here the Burke and SMRT models present again an almost equivalent output, even though the latter shows a better agreement with the UWBRAD measurements, specially when considering the Vant formulation. Furthermore, in this case even the Wilheit model is capable of reproducing the increase on TB,

but with more bias compared to the other radiative transfer models. It also does not show the oscillations observed in Figure 7.

Figure 10 shows the relative difference of comparing the modeled brightness temperature using different models and permittivity formulations with the UWBRAD in situ measurements during late 2019, from 4th to 13th December. All configurations using the Burke and SMRT models combined with the Vant or the random needles formulations present similar metrics, as expected from Figure 7. However, the Vant permittivity is slightly superior compared to the random needles, and the same can be argued for SMRT compared to Burke.

In Demir and others (2022a), a good match is found between UWBRAD measurements in this period and a multilayer, incoherent radiative transfer model that includes a snow layer, a second year ice layer (given the low salinity of the upper ice column, 0.4), a first year layer to model the measured accretion of ice to the base of the column, and the ocean. Ice growth from about

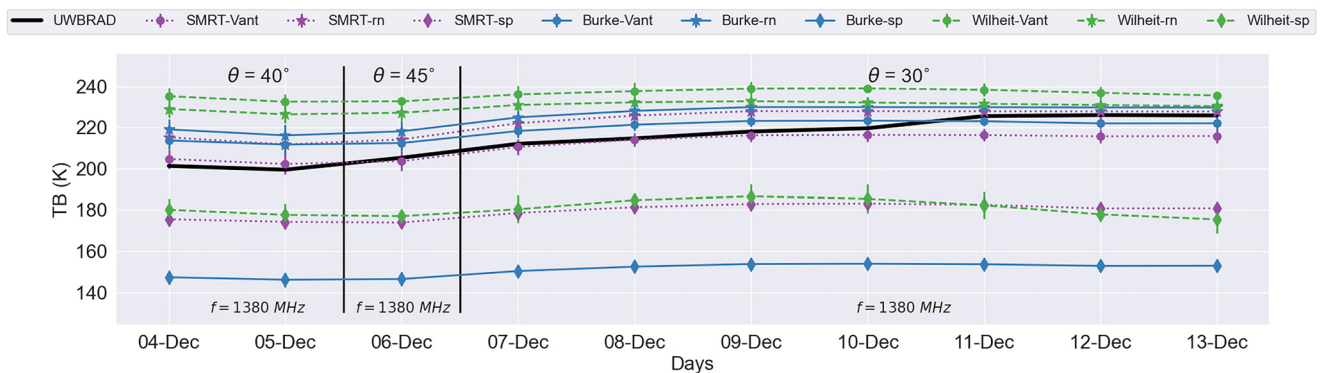


Figure 9. Temporal evolution of the UWBRAD brightness temperature modeled with the combination of the CFDD simulation and the Burke, SMRT and Wilheit models, along with the UWBRAD's first period measurements.

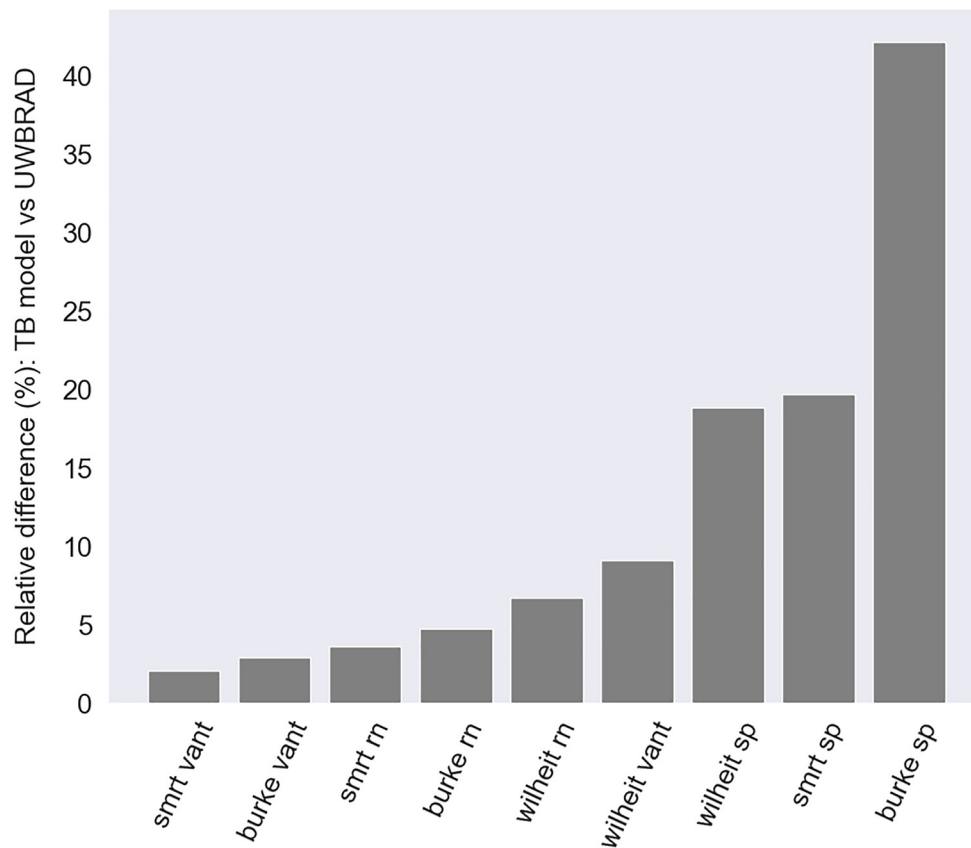


Figure 10. Relative difference of the modeled brightness temperature from the Burke, SMRT and Wilheit models assuming different permittivities with respect to the in situ UWBRAD measurements during the first period.

67 cm to 78 cm was observed during the coincident DTC observations.

Taking advantage of SMRT's capacity to consider multiple layers, Figure 11 shows the approach employed in this study and compares it with the approach suggested by Demir and others (2022a). The latter involves the incorporation of a saline first-year ice layer underneath a desalinated thicker layer, assumed to be growing up to 8.3 cm during the studied period. The TB increasing trend is similarly well reproduced by both approaches, indicating that it can be reproduced either by the increase in depth of the saline layer, or considering only one ice layer with a salinity approaching the average of both the desalinated and growing saline layers.

For the early winter UWBRAD measurements, from 18th to 23rd January, the temporal evolution is presented in Figure 12.

In this period the instruments measured at a fixed incidence angle of 35° , and the modeled TB is also integrated over the whole antenna pattern as done for the first period. The models are not able to follow the trend observed by the instrument, although the values are similar. It can be hypothesized that, as in January the ice is more consolidated and thus thicker than 1 m, as seen in Figure 6, it is out of the sensitivity range of the models at this frequency band. Here again the Burke and SMRT models are almost equivalent, except when the sphere permittivity model is used for which the SMRT is much better than the others.

Figure 13 shows the relative difference of the different model configurations compared to the measured UWBRAD data for this period. The differences remain similar to those for early December, as well as the best model configurations, although

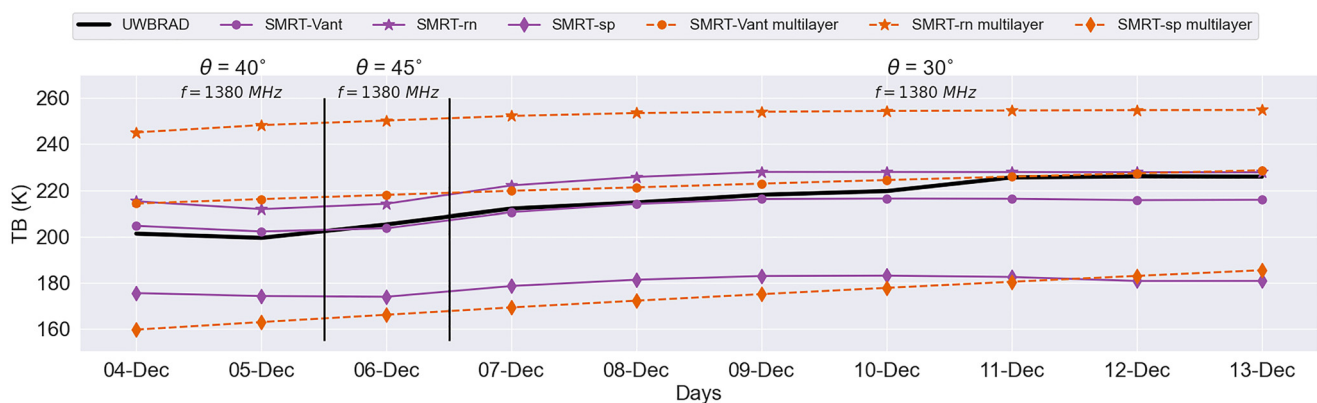


Figure 11. Temporal evolution of the UWBRAD brightness temperature modeled with the combination of the CFDD simulation and the SMRT model considering different permittivities, along with the model approach proposed by Demir and others (2022a) denoted as *multilayer*.

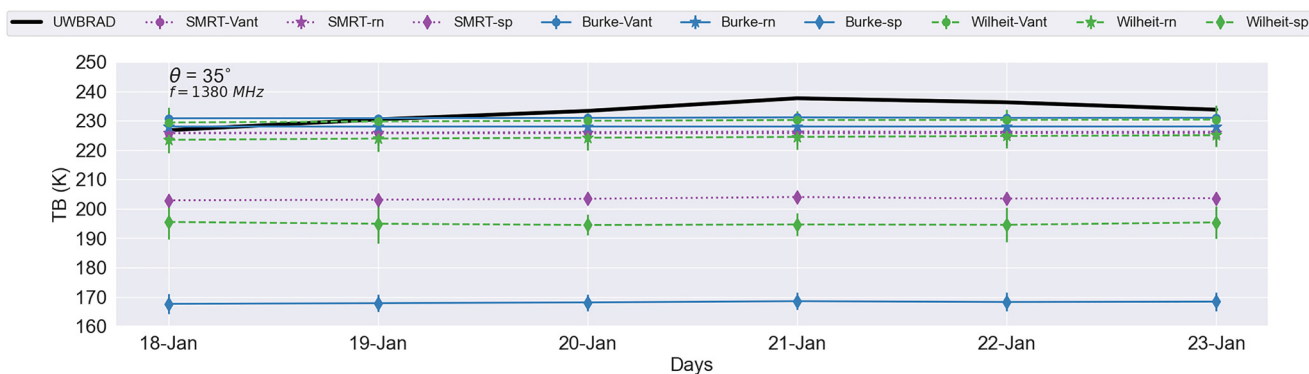


Figure 12. Temporal evolution of the brightness temperature modeled with the combination of the CFDD simulation and the Burke, SMRT and Wilheit models, along with the UWBRAD’s second period measurements.

the results are close between all the models assuming pure random needles or the Vant formulation.

4.2.3 Cross-instrument data analysis

Ultimately, a cross-instrument analysis is done to obtain an overall impression of how well the multiple modeling combinations match with the in situ data. The scatter plots in Figure 14 show how the radiative transfer models combined with the different permittivity formulations agree with all the ELBARA and UWBRAD measurements, gathering together all the periods in which they were operating. Even though the scatter plots show a quite similar behavior by Vant and random needles, the R^2 correlation coefficients indicate that random needles is the best permittivity formulation and spheres is the worse. The spheres permittivity results in extremely lower brightness temperatures

which are not physical for sea ice, specially when combined with the Burke model. Regarding the radiative transfer models, although it seemed that Burke and SMRT were close, here the metrics suggest the latter as better. Specifically, for lower TB the incoherent models are better, while the coherent agrees better with the in situ data at higher intensities.

5. Discussion

Starting with the sea ice growth simulation using the CFDD model, there is an overestimation of the sea ice thickness compared to the measurements from some ice coring profiles, and an underestimation of around 5 to 10 cm compared to the DTC data. These discrepancies can enlarge the difference of the posterior computation of the brightness temperature using the radiative

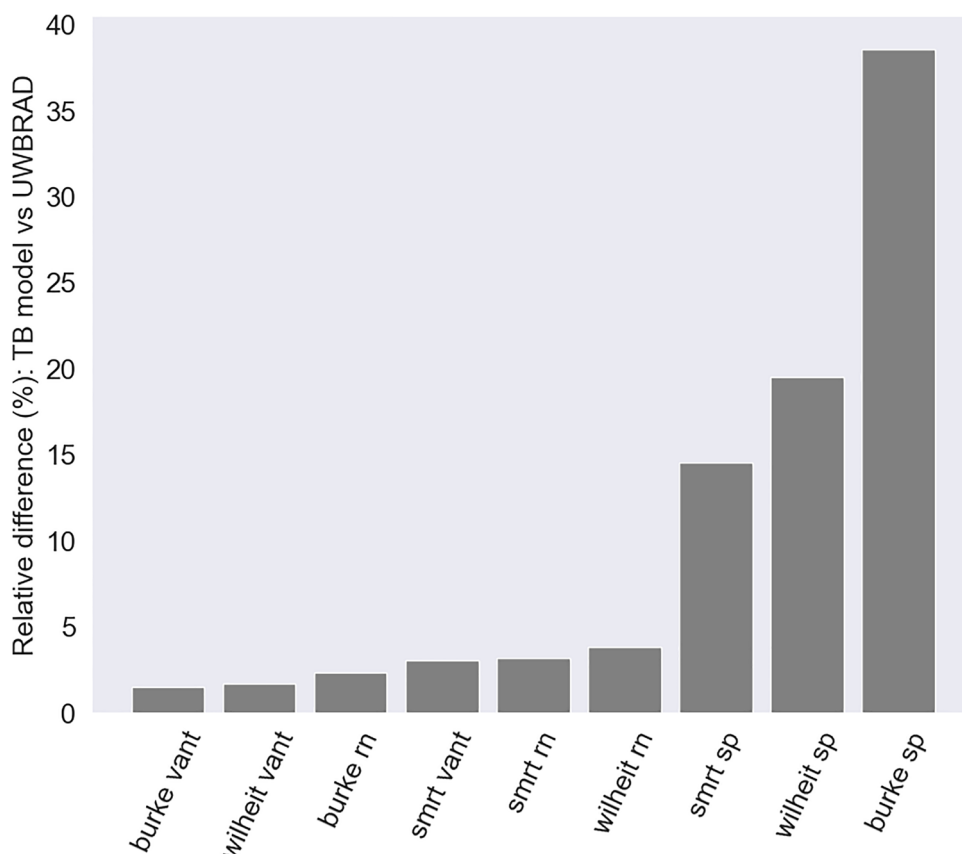


Figure 13. Relative difference of the modeled brightness temperature from the Burke, SMRT and Wilheit models assuming different permittivities with respect to the in situ UWBRAD measurements during the second period.

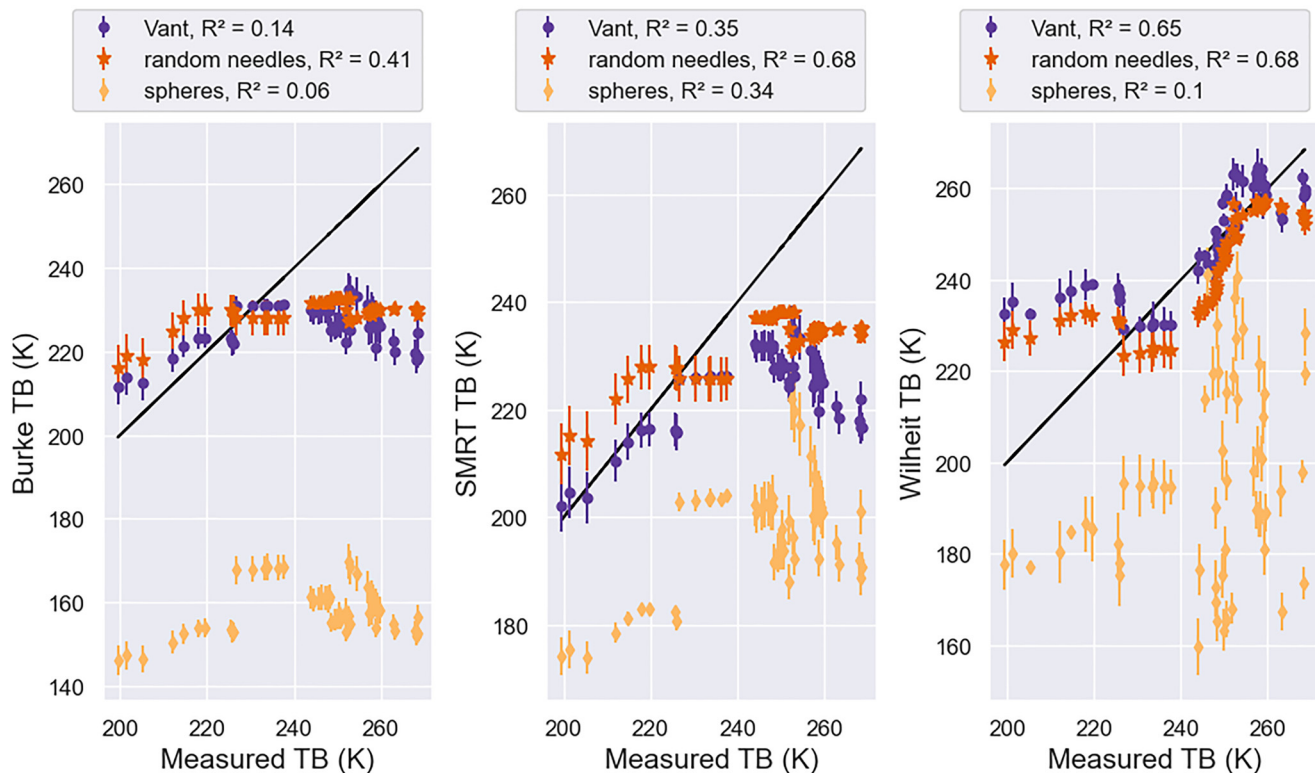


Figure 14. Scatter plots of the brightness temperature modeled with the different configurations as function of the combined ELBARA and UWBRAD measurements from all the periods, along with their respective correlation coefficient.

transfer models. This is reasonable considering the simplicity of the model, as it only accounts for the growing and neither melting nor decrease of the thickness is possible. The CFDD-simulated sea ice temperature is clearly deviated from the ground truth observations, presenting a similar trend but much lower bulk temperatures, of around 5 to 10 °C less. This can be associated to the insulation effect of the snow above ice. The DTC-derived temperature remains much closer to the ice coring, justifying its use in the modeled brightness temperature computation. The sea ice salinity is slightly deviated, but the trend seems to be well reproduced being constant. Therefore, the major source of uncertainty in this case is the sea ice temperature, due to its observed variability. It can present a wide range of values producing an important impact in the TB, while the sea ice salinity is shown to be almost constant and the thickness is well reproduced by a common growth for that time of the year. For these reasons, the error bars are computed as the difference between the model simulation with the DTC-derived and with the CFDD-derived sea ice temperatures. This approach considers the spatial variability of this variable, whereas sea ice thickness and salinity conditions are generally more uniform.

Regarding the radiometric data analysis, it is worth mentioning that for almost every period the different radiative transfer models obtain similar results when assuming the same permittivity formulation. Namely, the permittivity modeling seems to have a greater impact on the output brightness temperature than the approach, incoherent or coherent, of the radiative model. Noteworthy, although assuming spherical brine inclusions results in an unrealistic permittivity, an important difference between combining it with the SMRT model compared to the others is shown. Furthermore, the coherence effects included in the in the Wilheit model also lead to better results than the Burke model, probably because greater brightness temperatures can be reached with the model's predicted phase oscillations, as shown in Figure 2, although these oscillations are not evident in the

measurements. Despite the fact that the scattering is negligible at this low frequency, Burke model predicted brightness temperatures remain lower than those of the SMRT. It can be hypothesized that it is because the Burke model misses a fundamental contribution to the emission which involves the snow layer. Specifically, it does not account for the radiation coming from the ice being reflected from the snow bottom and then re-reflected again at the snow bottom that is finally transmitted through the snow top. The effect of neglecting these high order reflections is enhanced when considering the spheres formulation, as the difference with SMRT is much higher. This results in an average difference between Burke and SMRT of around 30 K when assuming spheres, while is kept below 5 K when random needles or Vant is used.

Figures 7, 9 and 12 suggest that, except for TBH measured by ELBARA during the sea ice growth period, where no model is able to well reproduce the in situ data, the in situ values lay within the region between each model's result when considering spheres and random needles. As one could expect, this indicates that the optimal permittivity should be somewhere between these theoretical formulations. The situation where the brine inclusions are perfect spheres or randomly-oriented needles, or even homogeneous, seems to be unrealistic for the naturally grown sea ice, and thus it could make sense to model them as imperfect and heterogeneous. Additionally, although the Vant formulation could be seen as the appropriate permittivity to be used as it was empirically derived and presents robust results as shown, its coefficients are interpolated to L-band and thus uncertainty is introduced.

Significant oscillations in the Wilheit model, particularly when paired with the spheres formulation, are evident in Figure 7, but not in Figures 9 and 12. For the latter, the oscillations are averaged out by integrating the model predictions for the different incidence angles over the UWBRAD antenna pattern. These oscillations are because of the coherence effects considered in this model, as illustrated in Figure 1. The choice of

permittivity is linked to these jumps, with the spheres and Vant formulations displaying oscillations across a wider range of sea ice conditions (see Figure 2). Again it is noted that no clear evidence of oscillatory behaviors in the measured brightness temperatures is observed.

The modeled brightness temperature for UWBRAD's first period presents great agreement with the in situ observations, following the TB increasing trend when considering almost every model configuration, except those with the Wilheit model or the spheres permittivity. This suggests that, even though the models were driven by sparsely sampled physical property measurements, the problem of infrequent time sampling is partially addressed using frequent DTC temperature sensor strings embedded in the ice, providing frequent temperature profile data. Moreover, once the temperature reaches the melting point, the ice thickness can be inferred. Salinity measurements over time are less frequent as weekly core data were used. In Demir and others (2022a), similarly to this paper's analysis, the model was applied to the time varying physical properties, obtaining also a good agreement between the model and the brightness temperature for the period from December 4 to December 14 (see Fig. 10 in Demir and others, 2022a). Therefore, the two different approaches to the sea ice layering model lead to similar great results.

Despite the fact that the middle part of Figures 7 and 9 show the same period of measurements, the UWBRAD results are increasing, in contrast to ELBARA. Although they could not be comparable because of their incompatible incidence angle of observation, this important disparity indicates the spatial variability on the sea ice conditions. As shown, these variations are mostly on the sea ice temperature, and this could produce the differences observed in the measured brightness temperature, even with both instruments operating nearby. Finally, Figure 6 indicates that the ice in the UWBRAD's early winter period was thicker than 1 m, for which the models at this frequency may not have sensitivity, as the saturation zone (see Figure 1) may have been reached given the ice conditions. However, the results could be acceptable considering that the sample is too small to observe any trend, producing a bias in the correlation coefficient. This is enhanced by Figure 13, which generally shows small relative differences for the modeled brightness temperatures, except when considering the spheres permittivity formulation.

6. Conclusions

The MOSAiC expedition was a unique opportunity to gather valuable data about the Arctic environment. Specially, the data collected by the L-band radiometers such as ELBARA and UWBRAD, can help to improve understanding of sea ice emission modeling which is key for the retrieval of geophysical parameters using remote sensing observations. The data from these instruments have been successfully handled to perform a comparison with three different radiative transfer models, in combination with three distinct permittivity formulations. From this analysis, multiple conclusions can be extracted.

Regarding the analysis of the different radiative transfer models, it is shown that Burke and SMRT present a similar behavior, as scattering can be neglected at a low frequency. Nevertheless, the Burke model is seen to be strictly lower as it does not include the contributions to the emission from higher order reflections that happen within the snow-ice interface. This is highly enhanced when both models consider the spheres permittivity, as a more important difference between them appears, reaching up to 25 K more than when random needles or Vant is considered. The coherent approach used in the Wilheit model is the only approach capable of reproducing the high TBH values, even the larger than TBV observed by ELBARA in the first days of the sea ice growth

period. Although it can be argued that this unusual high values are not physically realistic, for the other periods where the TBH measurements are nominal and generally the models predict lower values, the Wilheit model presents the most similar results. While this may suggest the presence of coherent effects, the oscillatory brightness temperatures that would result are not clearly observed in the measurements. Nevertheless, when modeling the UWBRAD measurements there is no major distinction between the two approaches. It can be said that incoherent models show slightly better results for the vertical polarization, with only around 1% less difference with the in situ observations compared to the coherent approach. However, they present worse results for the horizontal component and so at intensity overall, with approximately 10% more difference with the in situ measurements compared with the coherent model.

Focusing on the permittivity modeling, the widely used Vant empirical formulation is shown to be a robust option, as it presents reasonable results in every period, both for ELBARA and UWBRAD. However, for the ELBARA measurements specifically, the random needles formulation has better metrics. Assuming the brine inclusions as perfect spherical inclusions results in an unrealistic behavior on reproducing the in situ radiometric measurements. Ultimately, this study suggest that the more realistic permittivity lays within the range between the spheres and the random needles formulation, for which future field measurements can help in order to derive a new empirical formulation specifically for L-band.

In summary, these findings have implications for sea ice emission modeling and highlight the need for more in situ measurements to improve the current permittivity formulations, along with the importance of considering the coherence effects that are currently neglected at L-band remote sensing applications.

Acknowledgements. This project is funded from the AEI with the ARCTIC-MON project (PID2021-125324OB-I00) and also with the Programación Conjunta Internacional project called 'MEJORANDO LOS MODELOS DE EMISIVIDAD DEL HIELO MARINO EN LAS MICROONDAS DE BAJA FRECUENCIA' (ICE-MOD), with reference PCI2019-111844-2. This work represents a contribution to the CSIC Thematic Interdisciplinary Platform PTI-POLARCSIC and PTI-TELEDETECT and is supported by the Spanish government through the 'Severo Ochoa Centre of Excellence' accreditation (CEX2019-000928-S). Remote sensing data processing has been executed at the Barcelona Expert Center on Remote Sensing (BEC-RS, <https://bec.icm.csic.es>) of the Institut de Ciències del Mar ICM-CSIC. This work has been conducted in the framework of the PhD in Computer Science program of the Universitat Autònoma de Barcelona (UAB). This work is part of a Doctorat Industrial (AGAUR), with expedient number 2023 DI 0007.

References

- Angelopoulos M and 14 others (2022) Physical properties of sea ice cores from site BGCI measured on legs 1 to 3 of the MOSAiC expedition. PANGAEA. doi: [10.1594/PANGAEA.943768](https://doi.org/10.1594/PANGAEA.943768)
- Angelopoulos M and 26 others (2022) Deciphering the properties of different arctic ice types during the growth phase of MOSAiC: implications for future studies on gas pathways. *Frontiers in Earth Science* **10**. doi: [10.3389/feart.2022.864523](https://doi.org/10.3389/feart.2022.864523)
- Assur A (1960) Composition of sea ice and its tensile strength. Technical report, Technical report, U.S. Army Snow, Ice and Permafrost Research Establishment, Wilmette, Ill.
- Billelo M (1961) Formation, growth, and decay of sea-ice in the Canadian Arctic Archipelago. *Arctic*.
- Burke W, Schumge T and Paris J (1979) Comparison of 2.8- and 21-cm microwave radiometer observations over soils with emission model calculations. *Journal of Geophysical Research* **84**, 287–294. doi: [10.1029/JC084iC01p00287](https://doi.org/10.1029/JC084iC01p00287)
- Cox GFN and Weeks WF (1988) Numerical simulations of the profile properties of undeformed first-year sea ice during the growth season. *Journal of Geophysical Research: Oceans* **93**(C10), 12449–12460. doi: [10.1029/JC093iC10p12449](https://doi.org/10.1029/JC093iC10p12449)

- Demir O and Johnson J** (2021a) Arctic Sea Ice Thermal Emission Measurements from the Ultra Wideband Microwave Radiometer (UWBRAD) at the Multidisciplinary Drifting Observatory for the Study of Arctic Climate (MOSaIC) Expedition in December 2019. *Arctic Data Center*. doi: [10.18739/A2M03XZ32](https://doi.org/10.18739/A2M03XZ32)
- Demir O and Johnson J** (2021b) Arctic Sea Ice Thermal Emission Measurements from the Ultra Wideband Microwave Radiometer (UWBRAD) at the Multidisciplinary Drifting Observatory for the Study of Arctic Climate (MOSaIC) Expedition in January 2020. *Arctic Data Center*. doi: [10.18739/A2G737506](https://doi.org/10.18739/A2G737506)
- Demir O and 13 others** (2022a) Measurements of 540–1740 MHz brightness temperatures of sea ice during the winter of the MOSaIC campaign. *IEEE Transactions on Geoscience and Remote Sensing* **60**, 1–11. doi: [10.1109/TGRS.2021.3105360](https://doi.org/10.1109/TGRS.2021.3105360)
- Demir O and 6 others** (2022b) Studies of sea-ice thickness and salinity retrieval using 0.5–2 GHz microwave radiometry. *IEEE Transactions on Geoscience and Remote Sensing* **60**, 1–12. doi: [10.1109/TGRS.2022.3168646](https://doi.org/10.1109/TGRS.2022.3168646)
- Doronin Y** (1971) *Thermal Interaction of the Atmosphere and the Hydrosphere in the Arctic*. Philadelphia: Coronet Books.
- Entekhabi D and 22 others** (2010) The soil moisture active passive (SMAP) mission. *Proceedings of the IEEE* **98**(5), 704–716.
- Font J and 8 others** (2010) SMOS: the challenging sea surface salinity measurement from space. *Proceedings of the IEEE* **98**(5), 649–665. doi: [10.1109/JPROC.2009.2033096](https://doi.org/10.1109/JPROC.2009.2033096)
- Gabarró C and 12 others** (2022) First results of the ARIEL L-band radiometer on the MOSaIC Arctic expedition during the late summer and autumn period. *Elementa: Science of the Anthropocene* **10**(1), 00031. doi: [10.1525/elementa.2022.00031](https://doi.org/10.1525/elementa.2022.00031)
- Hersbach H and 14 others** (2020) ERA5 hourly data on single levels from 1940 to present. Copernicus Climate Change Service (C3S) Climate Data Store (CDS). doi: [10.24381/cds.adbb2d47](https://doi.org/10.24381/cds.adbb2d47)
- Heygster G, Huntemann M, Ivanova N, Saldo R and Pedersen LT** (2014) Response of passive microwave sea ice concentration algorithms to thin ice. In *2014 IEEE Geoscience and Remote Sensing Symposium*, 3618–3621.
- Huntemann M and 5 others** (2014) Empirical sea ice thickness retrieval during the freeze-up period from SMOS high incident angle observations. *The Cryosphere* **8**, 439–451. doi: [10.5194/tc-8-439-2014](https://doi.org/10.5194/tc-8-439-2014)
- Huntemann M** (2015) *Thickness retrieval and emissivity modeling of thin sea ice at L-band for SMOS satellite observations*. Ph.D. thesis.
- Jezek KC and 13 others** (2019) Remote sensing of sea ice thickness and salinity with 0.5–2 GHz microwave radiometry. *IEEE Transactions on Geoscience and Remote Sensing* **57**(11), 8672–8684. doi: [10.1109/TGRS.2019.2922163](https://doi.org/10.1109/TGRS.2019.2922163)
- Johnson JT and 15 others** (2016) The Ultra-wideband Software-Defined Radiometer (UWBRAD) for ice sheet internal temperature sensing: Results from recent observations. In *2016 IEEE International Geoscience and Remote Sensing Symposium (IGARSS)*, 7085–7087. doi: [10.1109/IGARSS.2016.7730848](https://doi.org/10.1109/IGARSS.2016.7730848)
- Kaleschke L, Tian-Kunze X, Maaß N, Mäkynen M and Drusch M** (2012) Sea ice thickness retrieval from SMOS brightness temperatures during the Arctic freeze-up period. *Geophysical Research Letters* **39**, L05501. doi: [10.1029/2012GL050916](https://doi.org/10.1029/2012GL050916)
- Kerr Y and 14 others** (2010) The SMOS mission: new tool for monitoring key elements of the global water cycle. *Proceedings of the IEEE IGARSS 2010*, no. 5, **98**, 666–687.
- Klein L and Swift C** (1977) An improved model for the dielectric constant of sea water at microwave frequencies. *IEEE Transactions on Antennas and Propagation* **AP-25**(1), 104–111.
- Kwok R** (2018) Arctic sea ice thickness, volume, and multiyear ice coverage: losses and coupled variability (1958–2018). *Environmental Research Letters* **13**(10), 105005. doi: [10.1088/1748-9326/aae3ec](https://doi.org/10.1088/1748-9326/aae3ec)
- Maass N, Kaleschke L, Tian-Kunze X and Tonboe RT** (2015) Snow thickness retrieval from L-band brightness temperatures: a model comparison. *Annals of Glaciology* **56**(69), 9–17. doi: [10.3189/2015AoG69A886](https://doi.org/10.3189/2015AoG69A886)
- Mätzler C** (1996) Microwave permittivity of dry snow. *Geoscience and Remote Sensing, IEEE Transactions on* **34**(2), 573–581. doi: [10.1109/36.485133](https://doi.org/10.1109/36.485133)
- Mätzler C** (2006) *Thermal Microwave Radiation: Applications For Remote Sensing*. Institute Of Electrical Engineers.
- Mecklenburg S, Wright N, Bouzina C and Delwart S** (2009) Getting down to business - SMOS operations and products. *ESA Bulletin* **137**, 25–30.
- Naderpour R and Schwank M** (2021) Sled-mounted ELBARA-III in MOSaIC expedition: measurement and data processing report. technical report.
- Nakawo M and Sinha NK** (1981) Growth rate and salinity profile of first-year sea ice in the high Arctic. *Journal of Glaciology* **27**(96), 315–330. doi: [10.3189/S0022143000015409](https://doi.org/10.3189/S0022143000015409)
- Nicolaus M and 103 others** (2022) Overview of the MOSaIC expedition: snow and sea ice. *Elementa: Science of the Anthropocene* **10**(1), 000046. doi: [10.1525/elementa.2021.000046](https://doi.org/10.1525/elementa.2021.000046)
- Picard G, Sandells M and Löwe H** (2018) SMRT: an active-passive microwave radiative transfer model for snow with multiple microstructure and scattering formulations (v1.0). *Geoscientific Model Development* **11**(7), 2763–2788. doi: [10.5194/gmd-11-2763-2018](https://doi.org/10.5194/gmd-11-2763-2018)
- Salganik E, Hoppmann M, Scholz D, Haapala J and Spreen G** (2023a) Temperature after the cooling cycle from the sea ice mass balance buoy DTC12 during MOSaIC 2019/2020. PANGAEA. doi: [10.1594/PANGAEA.962441](https://doi.org/10.1594/PANGAEA.962441), in: Salganik E and others (2023): Temperature and heating induced temperature difference measurements from the sea ice mass balance buoy DTC12 during MOSaIC 2019/2020. PANGAEA. doi: [10.1594/PANGAEA.962434](https://doi.org/10.1594/PANGAEA.962434)
- Salganik E and 6 others** (2023b) Temperature after the cooling cycle from the sea ice mass balance buoy DTC20 during MOSaIC 2019/2020. PANGAEA. doi: [10.1594/PANGAEA.962452](https://doi.org/10.1594/PANGAEA.962452), in: Salganik E and others (2023): Temperature and heating induced temperature difference measurements from the sea ice mass balance buoy DTC20 during MOSaIC 2019/2020. PANGAEA. doi: [10.1594/PANGAEA.962450](https://doi.org/10.1594/PANGAEA.962450)
- Schwank M and 7 others** (2010) ELBARA II, an L-band radiometer system for soil moisture research. *Sensors* **10**(1), 584–612. doi: [10.3390/s100100584](https://doi.org/10.3390/s100100584)
- Shokr M** (1998) Field observations and model calculations of dielectric properties of Arctic sea ice in the microwave C-band. *IEEE Transactions on Geoscience and Remote Sensing* **36**(2), 463–478. doi: [10.1109/36.662730](https://doi.org/10.1109/36.662730)
- Stogryn A and Desargant G** (1985) The dielectric properties of brine in sea ice at microwave frequencies. *IEEE Transactions on Antennas and Propagation* **33**(5), 523–532. doi: [10.1109/TAP.1985.1143610](https://doi.org/10.1109/TAP.1985.1143610)
- Tiuri M, Sihvola A, Nyfors E and Hallikaiken M** (1984) The complex dielectric constant of snow at microwave frequencies. *IEEE Journal of Oceanic Engineering*, **9**(5), 377–382. doi: [10.1109/JOE.1984.1145645](https://doi.org/10.1109/JOE.1984.1145645)
- Vant M, Ramseier R and Makios V** (1978) The complex-dielectric constant of sea ice at frequencies in the range 0.1–40 GHz. *Journal of Applied Physics* **49**, 1264–1280.
- Warren SG and 6 others** (1999) Snow depth on Arctic sea ice. *Journal of Climate* **12**(6), 1814–1829. doi: [10.1175/1520-0442\(1999\)012<1814:SDOASI>2.0.CO;2](https://doi.org/10.1175/1520-0442(1999)012<1814:SDOASI>2.0.CO;2)
- Weeks W** (2010) *On Sea Ice*. Fairbanks: University of Alaska Press.
- Wilheit TT** (1978) Radiative transfer in a plane stratified dielectric. *IEEE Transactions on Geoscience Electronics* **16**(2), 138–143. doi: [10.1109/TGE.1978.294577](https://doi.org/10.1109/TGE.1978.294577)